Available online at www.sciencedirect.com
ScienceDirect
Acta Materialia 59 (2011) 7029–7042
Acta MATERIALIA
www.elsevier.com/locate/actamat

Coarsening resistance at 400 °C of precipitation-strengthened Al–Zr–Sc–Er alloys

Christopher Booth-Morrison [a,*], David C. Dunand [a], David N. Seidman [a,b,*]

[a] Department of Materials Science and Engineering, Northwestern University, Evanston, IL 60208, USA
[b] Northwestern University Center for Atom-Probe Tomography (NUCAPT), Evanston, IL 60208, USA

Received 31 May 2011; received in revised form 25 July 2011; accepted 27 July 2011
Available online 23 August 2011

Abstract

The effect of substituting 0.01 or 0.02 at.% Er for Sc in an Al–0.06 Zr–0.06 Sc at.% alloy was studied to develop cost-effective high-temperature aluminum alloys for aerospace and automotive applications. Spheroidal, coherent, $L1_2$-ordered $Al_3(Sc, Zr, Er)$ precipitates with a structure consisting of an Er-enriched core surrounded by a Sc-enriched inner shell and a Zr-enriched outer shell (core/double-shell structure) were formed after aging at 400 °C. This core/double-shell structure strengthens the alloy, and renders it coarsening resistant for at least 64 days at 400 °C. This structure is formed due to sequential precipitation of solute elements according to their diffusivities, D, where $D_{Er} > D_{Sc} > D_{Zr}$ at 400 °C. Zr and Er are effective replacements for Sc, accounting for 33 ± 1% of the total precipitate solute content in an Al–0.06 Zr–0.04 Sc–0.02 Er at.% alloy aged at 400 °C for 64 days. Er accelerates precipitation kinetics at 400 °C, resulting in: (i) strengthening due to the elimination of lobed-cuboidal precipitates in favor of spheroidal precipitates; and (ii) a decrease in the incubation time for nucleation because $D_{Er} > D_{Sc}$. Finally, a two-stage aging treatment (24 h at 300 °C + 8 h at 400 °C) provides peak microhardness due to optimization of the nanostructure.

Keywords: Aluminum alloys; Precipitation; Scandium; Zirconium; Erbium

1. Introduction

Cast dilute Al–Zr–Sc alloys, where Sc and Zr are below their solubility limits, are excellent candidates for certain high-temperature automotive and aerospace applications where cast iron and titanium alloys are currently the materials of choice. Al–Zr–Sc alloys offer promising strength and creep resistance at temperatures >300 °C, and can be produced affordably using conventional casting and heat treatment [1]. Upon aging, supersaturated Al–Sc alloys form coherent $L1_2$-ordered Al_3Sc precipitates, which provide significant strengthening to a temperature of ~300 °C [2–7]. Zr is added to Al–Sc alloys to form coarsening-resistant $Al_3(Sc_xZr_{1-x})$ ($L1_2$) precipitates, which consist of a Sc-enriched core surrounded by a Zr-enriched shell [8–20]. The industrial applicability of Al–Sc alloys is limited, however, by the high cost of Sc, motivating the replacement of as much Sc as is possible with other solute elements, such as rare-earth (RE) elements [1,7,21–26]. The substitution of Sc with the lower-cost RE element Er has proven effective in maintaining the high-temperature strength, and improving the creep resistance, of Al–Sc alloys at 300 °C [21–23]. The substitution of Yb for Sc in the Al–Sc–Zr system was found to improve the creep properties of the alloy, while maintaining the coarsening resistance due to Zr [27]. Er is used herein because it is the least expensive of the heavy RE $L1_2$ precipitate formers [28], and Al_3Er ($L1_2$) has the largest lattice parameter misfit with Al ($\delta = +4.08\%$) [29], thereby improving creep resistance by enhancing elastic interactions with dislocations [22,30].

In this article, we address the design of high-temperature Al–Zr–Sc–Er alloys, focusing on the optimization of both

* Corresponding authors.
E-mail addresses: c-booth@northwestern.edu (C. Booth-Morrison), d-seidman@northwestern.edu (D.N. Seidman).

1359-6454/$36.00 © 2011 Acta Materialia Inc. Published by Elsevier Ltd. All rights reserved.
doi:10.1016/j.actamat.2011.07.057

alloy composition and heat treatment. The principal design requirements are as follows: (i) high-temperature strength and coarsening resistance; (ii) control of precipitate coherency; (iii) minimization of grain refinement, to limit diffusional creep; and (iv) affordability. High-temperature strength and control of precipitate coarsening and coherency are achieved by selecting an alloy composition that yields a large number density of nanometer-scale spheroidal core/shell precipitates. A Zr concentration of 0.06 at.% is chosen because it has been shown to be effective in retarding coarsening and avoiding loss of coherency with the matrix [31,32]. Previous work on Al–Zr–Sc alloys has shown that a total solute concentration below ~0.15 at.% results in millimeter–diameter grains upon casting by eliminating primary precipitates, which can inhibit grain growth after solidification and/or during homogenization [10,18,31–40]. Large grains minimize grain-boundary sliding, which becomes an active creep mechanism at elevated temperatures. Thus, a Sc concentration of 0.06 at.% is chosen to provide significant precipitation hardening, while eliminating the possibility of primary precipitation and concomitant small grain diameters. The need to control cost in Al–Zr–Sc alloys dictates the replacement of Sc with the lower-cost Er. Given that the solubility of Er in binary Al–Er is 0.046 at.% at 640 °C [25], an Er concentration of no more than 0.02 at.% is studied to minimize the risk of primary precipitation.

The optimization of both the chemical composition and heat treatment of Al–Zr–Sc–Er alloys is performed with the goal of developing Al alloys capable of replacing cast iron and titanium alloys in existing automotive and aerospace applications in the 200–400 °C temperature range. Beginning with a base Al–0.06 Zr–0.06 Sc at.% alloy, the effect of substituting 0.01 and 0.02 at.% Er for Sc on strength and precipitate evolution is studied by microhardness, electrical conductivity, atom-probe tomography (APT), scanning electron microscopy (SEM) and transmission electron microscopy (TEM).

2. Experimental

2.1. Alloy compositions and processing

A ternary and two quaternary alloys were cast, with nominal compositions of Al–0.06 Zr–0.06 Sc, Al–0.06 Zr–0.05 Sc–0.01 Er and Al–0.06 Zr–0.04 Sc–0.02 Er at.%, respectively. Their compositions in the as-cast state are given in Table 1, as measured by direct current plasma emission spectroscopy (DCPMS) (ATI Wah Chang, Albany, OR). The Si and Fe content of the alloys was less than the 0.005 and 0.0025 at.% detection limit, respectively, of the DCPMS technique.

The alloys were dilution cast from 99.999 at.% pure Al (Alfa Aesar, Ward Hill, MA) and Al–0.9 at.% Sc, Al–0.6 at.% Zr and Al–1.15 at.% Er master alloys. The Al–Sc and Al–Zr master alloys were themselves dilution cast from commercial Al–1.3 at.% Sc (Ashurst Technology, Ltd., Baltimore, MD), and Al–3 at.% Zr (KB Alloys, Reading, PA) master alloys. The Al–Er master alloy was prepared by melting 99.999 at.% pure Al with 99.99 at.% Er (Stanford Materials Corporation, Aliso Viejo, CA) using non-consumable electrode arc-melting in a gettered purified-argon atmosphere (Atlantic Equipment Engineers, Bergenfield, NJ). To create the final dilute alloys, the master alloys and 99.999 at.% pure Al were melted in flowing argon in zirconia-coated alumina crucibles in a resistively heated furnace at 850 °C. The master alloys were preheated to 640 °C to accelerate solute dissolution and minimize solute losses from the melt. The melt was held in a resistively heated furnace for 7 min at 850 °C, stirred vigorously, and then cast into a graphite mold preheated to 200 °C. During solidification, the mold was chilled by placing it on an ice-cooled copper platen to encourage directional solidification and discourage the formation of shrinkage cavities.

The castings were homogenized in air at 640 °C for 72 h and then water quenched to ambient temperature. Three separate aging studies were conducted: (i) isochronal aging in stages of 25 °C h^{-1} for temperatures from 100 to 600 °C; (ii) isothermal aging at 400 °C for times ranging from 0.5 min to 256 days (8 months); and (iii) two-stage isothermal aging consisting of a first heat treatment at 300 °C for 24 h followed by aging at 400 °C for times ranging from 0.5 h to 64 days. Molten salt ($NaNO_2$–$NaNO_3$–KNO_3) baths were used for aging durations <0.5 h to ensure rapid heat transfer, while longer aging experiments were performed in air.

2.2. Analytical techniques

The homogenized microstructure of unetched samples polished to a 1 μm surface finish was imaged by SEM using a Hitachi S3400N-II microscope, equipped with an Oxford

Table 1
Compositions (at.%) of the alloys investigated, as measured by direct current plasma emission spectroscopy (DCPMS) and local-electrode atom-probe (LEAP) tomography. The reported LEAP tomographic compositions are averages of at least two samples for each alloy. Measurement uncertainty is given in parenthesis after the significant digit to which it applies.

Nominal	Measured alloy composition (DCPMS)			Measured alloy composition (LEAP)		
	Zr	Sc	Er	Zr	Sc	Er
Al–0.06 Zr–0.06 Sc	0.052 (1)	0.067 (1)	–	0.0256 (7)	0.0685 (9)	–
Al–0.06 Zr–0.05 Sc–0.01 Er	0.035 (1)	0.047 (1)	0.010 (1)	0.0198 (7)	0.0476 (8)	0.0038 (4)
Al–0.06 Zr–0.04 Sc–0.02 Er	0.035 (2)	0.042 (1)	0.019 (1)	0.0200 (7)	0.0394 (5)	0.0046 (4)

Instruments INCAx-act detector for energy-dispersive X-ray spectroscopy (EDS). The precipitate morphology was studied using a Hitachi 8100 transmission electron microscope at 200 kV. TEM foils were prepared by grinding aged specimens to a thickness of 100–200 μm, from which 3 mm diameter disks were punched. These disks were thinned by twin-jet electropolishing at ~20 V DC using a Struers TenuPol-5 with a 10 vol.% solution of perchloric acid in methanol at −40 °C.

Precipitation in these alloys was monitored by Vickers microhardness and electrical conductivity measurements. Vickers microhardness measurements were performed on a Duramin-5 microhardness tester (Struers) using a 200 g load applied for 5 s on samples polished to a 1 μm surface finish. Fifteen indentations were made per specimen across several grains. Electrical conductivity measurements were performed using a Sigmatest 2.069 eddy current instrument (Foerster Instruments, Pittsburgh, PA) at frequencies of 120, 240, 480 and 960 kHz.

Specimens for three-dimensional (3-D) local-electrode atom-probe (LEAP) tomography were prepared by cutting blanks with a diamond saw to approximate dimensions of $0.35 \times 0.35 \times 10\ mm^3$. These were electropolished at 8–20 V DC using a solution of 10% perchloric acid in acetic acid, followed by a solution of 2% perchloric acid in butoxyethanol at room temperature. Pulsed-laser APT was performed with a LEAP 4000X Si X tomograph (Cameca, Madison, WI) [41–47] at a specimen temperature of 35 K, employing focused picosecond UV laser pulses (wavelength = 355 nm) with a laser beam waist of <5 mm at the e^{-2} diameter. A laser energy of 0.075 nJ per pulse, a pulse repetition rate of 250 kHz, and an evaporation rate of 0.04 ions per pulse were used. LEAP tomographic data were analyzed with the software program IVAS 3.4.1 (Cameca). The matrix/precipitate heterophase interfaces were delineated with Sc isoconcentration surfaces, and compositional information was obtained with the proximity histogram methodology [48,49]. The measurement errors for all quantities were calculated based on counting statistics and standard error propagation techniques [50].

3. Results

3.1. As-homogenized microstructural analysis

The homogenized microstructure of the alloys consists of columnar grains with diameters of the order of 1–2 mm. SEM shows the presence of intragranular Al_3Zr flakes in all alloys, which are retained from the melt due to incomplete dissolution of the Al–Zr master alloy (Fig. 1a). The approximate composition of the flakes was obtained by semi-quantitative EDS, i.e. without rigorous calibration, which confirms the Al_3Zr stoichiometry, and reveals neither Er nor Sc in the flakes. These flakes were not found in previous arc-melted Al–0.06 Zr–0.06 Sc at.% and Al–1.0 Zr–1.0 Sc at.% alloys [31,32] due to the higher temperatures achieved during arc-melting. The differences

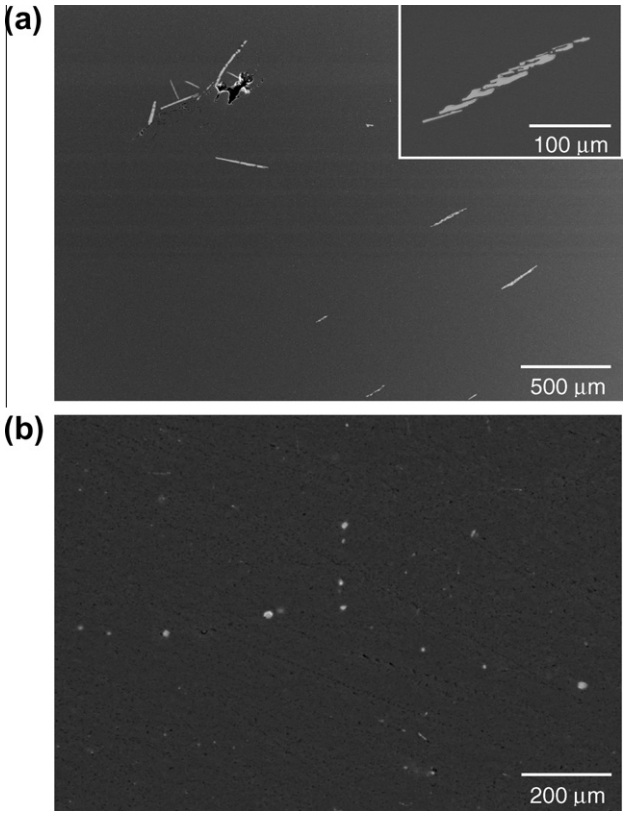

Fig. 1. SEM micrograph of the as-homogenized microstructure in (a) Al–0.06 Zr–0.06 Sc and (b) Al–0.06 Zr–0.05 Sc–0.01 Er. Flakes of Al_3Zr in (a) are retained from the melt due to incomplete dissolution of the Al–Zr master alloy, diminishing the matrix supersaturation of Zr. The intergranular Al_3Er ($L1_2$) primary precipitates imaged in (b) are undesirable because they deprive the matrix of Er, and can result in grain boundary pinning, preventing the coarse grain structures that are favorable for creep resistance. The approximate chemical composition of the flakes in (a) and precipitates in (b) were confirmed by semiquantitative EDS.

between the nominal and measured Zr concentrations of the alloys in Table 1 are a result of these Zr-rich flakes, which are not uniformly distributed in the alloys, and may have been excluded from the 300 mm^3 of material used for DCPMS. No Al_3Zr flakes were present in the small analysis volume of the LEAP tomographic reconstructions, and therefore the average of the measured Zr concentrations from the LEAP tomographic datasets of each alloy (Table 1) shows the Zr available in the matrix for precipitation during aging.

In the Er-containing alloys, intergranular Al_3Er ($L1_2$) primary precipitates were detected, and contained neither Zr nor Sc, as confirmed by EDS (Fig. 1b). Primary precipitation in these alloys decreases strength by depleting the matrix of solute, and, when excessive, can result in grain refinement, reducing the resistance to diffusional creep. The formation of primary precipitates in the homogenized samples indicates that the Er-containing alloys exceeded their solubility limit during solidification and homogenization. The addition of Sc and Zr has thus decreased the 0.046 at.% solubility of Er in binary Al–Er [25]. The analysis volume of the LEAP technique is too small to detect

intergranular Al_3Er, as was the case for the Al_3Zr flakes. The LEAP-tomographic measured compositions of Er of 0.0046 ± 0.0004 and 0.0038 ± 0.0004 at.% for Al–0.06 Zr–0.04 Sc–0.02 Er and Al–0.06 Zr–0.05 Sc–0.01 Er, are well below the nominal values of 0.02 and 0.01 at.% Er, respectively (Table 1). Only a fraction of the Er added to the alloys is available for nanoscale precipitation.

Previous research on arc-melted Al–0.06 Zr–0.06 Sc and Al–0.1 Zr–0.1 Sc at.% alloys revealed microsegregation of both Sc and Zr in the as-cast condition using linear composition profiles obtained employing quantitative electron-probe microanalysis (EPMA) [31,32]. The first solid to form in dilute Al–Zr–Sc alloys is enriched in Zr, resulting in a microstructure consisting of Zr-enriched dendrites surrounded by Sc-enriched interdendritic regions. The as-cast Al–0.06 Zr–0.06 Sc at.% alloy in the previous work showed a Zr enrichment of ~0.04 at.% Zr and a Sc depletion of ~0.01 at.% in the dendrites with respect to the average alloy composition, while the interdendritic region was depleted by ~0.04 at.% Zr and enriched by ~0.02 at.% Sc [31,32]. Microsegregation is expected in the present alloys, though to a lesser extent than in the previous Al–0.06 Zr–0.06 Sc and Al–0.1 Zr–0.1 Sc alloys, because the incomplete dissolution of the Al–Zr master alloy diminishes the effective Zr alloy concentration to 0.02–0.03 at.% (Table 1).

The degree of solute microsegregation in the present research is also diminished by homogenization at 640 °C for 72 h, which was not performed in prior work on Al–0.06 Zr–0.06 Sc due to concerns about primary precipitation of Al_3Zr [31]. In a similar study on Al–0.06 Sc, the microsegregation of Sc was completely eliminated by homogenization at 640 °C for 28 h [31]. Given that the diffusivity of Zr in Al, 1.0×10^{-15} m^2 s^{-1} [51], is significantly smaller than that of Sc in Al, 6.7×10^{-14} m^2 s^{-1} [52], at 640 °C (Table 2), homogenization of Zr requires heat-treatment durations that are impractically long. In summary, the effective Zr and Er concentrations of the alloys are smaller than their nominal values due to incomplete dissolution of the Al–Zr master alloy, and the formation of intergranular primary Al_3Er ($L1_2$) precipitates. In the following, we use the nominal compositions to label the alloys.

Table 2
Reported diffusivities of Zr, Sc and Er in Al at 300, 400 and 640 °C.

Temperature (°C)	D_{Zr} [51] (m^2 s^{-1})	D_{Sc} [52] (m^2 s^{-1})	D_{Er} [25] (m^2 s^{-1})
300	6.4×10^{-24}	9.1×10^{-20}	$(4 \pm 2) \times 10^{-19}$
400	1.2×10^{-20}	2.0×10^{-17}	–
640	1.0×10^{-15}	6.7×10^{-14}	–

3.2. Isochronal aging

The precipitation behavior of the ternary and quaternary alloys during isochronal aging in stages of 25 °C h^{-1} is displayed in Fig. 2, as monitored by Vickers microhardness and electrical conductivity. In Al–0.06 Zr–0.06 Sc, precipitation commences at 300 °C, as reflected by a sharp increase in the microhardness and electrical conductivity. The microhardness peaks for the first time at 350 °C and achieves a value of 582 ± 5 MPa, before decreasing to 543 ± 16 MPa at 400 °C. The microhardness increases again at 425 °C, achieving a second peak of 597 ± 16 MPa at 450 °C. The electrical conductivity increases continuously from 300 to 375 °C, before reaching a plateau at values of 33.94 ± 0.09 and 33.99 ± 0.09 MS m^{-1} for 375 and 400 °C. At 425 °C, the electrical conductivity increases to 34.75 ± 0.10 MS m^{-1}, reaching a peak of 34.92 ± 0.11 MS m^{-1} at 450 °C. Above 450 °C, both microhardness and electrical conductivity decrease quickly due to precipitate dissolution.

The first peak in the microhardness of Al–0.06 Zr–0.06 Sc at 325 °C occurs at the same temperature as the peak microhardness in recent studies of Al–0.06 Sc and Al–0.1 Sc alloys aged isochronally for 3 h for every 25 °C increase [31,32]. As such, the first peak in the microhardness we observe can be attributed to the precipitation of Al_3Sc. The second peak in the microhardness at 450 °C occurs at the same temperature as was previously found to produce a peak in the microhardness of an Al–0.1 Zr alloy aged isochronally for 3 h for every 25 °C increase [32]. The peak microhardness in an Al–0.06 Zr alloy was found to occur at 475 °C for samples aged isochronally for 3 h for every 25 °C increase [31]. The second peak in the microhardness is thus due to precipitation of Zr from the matrix. Previously studied Al–0.06 Zr–0.06 Sc and Al–0.1 Zr–0.1 Sc alloys aged isochronally for 3 h for every 25 °C increase were found to have only one peak in the microhardness, occurring at 400 °C [32]. The detection of only one peak in the microhardness was probably due to the smaller temporal resolution used in the previous studies, compared to the isochronal aging of 1 h for every 25 °C we employed.

The peak microhardness of the Er-containing alloys is smaller than that observed in Al–0.06 Zr–0.06 Sc. These results are consistent with isochronal microhardness results from Al–0.12 Sc and Al–0.9 Sc–0.03 Er alloys [53], where it was reasoned that the decrease in strength with the addition of Er was a result of solute consumption by primary precipitates, such as those in Fig. 1a. Nanoscale precipitation in the Er-containing alloys, as evidenced by increases in microhardness and conductivity, begins at temperatures as low as 200 °C, which is consistent with prior results on Al–Sc–Er alloys [53]. The microhardness values of the Er-containing alloys achieve plateaux between 325 and 450 °C. Beyond 450 °C, both microhardness and electrical conductivity decrease rapidly due to precipitate dissolution, as observed in Al–0.06 Zr–0.06 Sc. The electrical conductivity of homogenized Al–0.06 Zr–0.06 Sc of 31.5 ± 0.2 MS m^{-1} is significantly smaller than the values of 32.6 ± 0.2 and 33.0 ± 0.2 MS m^{-1} for Al–0.06 Zr–0.05 Sc–0.01 Er and Al–0.06 Zr–0.04 Sc–0.02 Er, respectively. This is a result of primary precipitation of Al_3Er ($L1_2$) in the Er-containing alloys, which deprives the matrix of solute and increases the electrical conductivity.

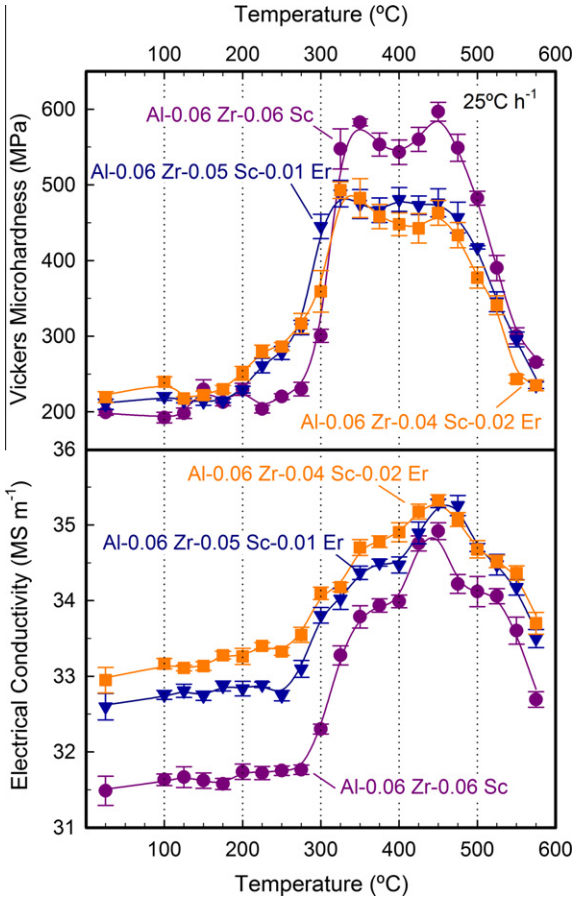

Fig. 2. Evolution of the Vickers microhardness and electrical conductivity during isochronal aging in stages of 25 °C h^{-1} for Al–0.06 Zr–0.06 Sc, Al–0.06 Zr–0.05 Sc–0.01 Er and Al–0.06 Zr–0.04 Sc–0.02 Er.

The nanostructures of Al–0.06 Zr–0.06 Sc and Al–0.06 Zr–0.04 Sc–0.02 Er aged isochronally to peak strength at 450 °C, and obtained from LEAP tomography, are displayed in Fig. 3. The Al–0.06 Zr–0.06 Sc alloy (Fig. 3a), has a number density of precipitates, N_v, of $2.1 \pm 0.2 \times 10^{22}$ m^{-3}, with an average radius, $\langle R \rangle$, of 3.1 ± 0.4 nm, and a volume fraction, ϕ, of $0.251 \pm 0.002\%$ (Table 3). The number density in Al–0.06 Zr–0.04 Sc–0.02 Er is smaller, $8.6 \pm 1.5 \times 10^{21}$ m^{-3}, with average radius and volume fraction values of 3.4 ± 0.6 nm and $0.157 \pm 0.003\%$, respectively. The number density and volume fraction of precipitates are smaller in the Er-containing alloy because the matrix solute supersaturation is smaller due to primary precipitation of Er during solidification and homogenization (Fig. 1). The concentration profiles across the matrix/precipitate interface obtained from the LEAP tomographic results (Fig. 3) are displayed in Fig. 4. As anticipated from previous results on similar alloys [8–16], the precipitates in Al–0.06 Zr–0.06 Sc consist of a Sc-enriched core surrounded by a Zr-enriched shell, with an average precipitate composition of 71.95 ± 0.10 at.% Al, 5.42 ± 0.05 at.% Zr and 22.63 ± 0.09 at.% Sc (Table 4). The precipitates in Al–0.06 Zr–0.04 Sc–0.02 Er consist of an Er-enriched core surrounded by a Sc-enriched inner shell and a Zr-enriched outer shell, with an average precipitate composition of 73.27 ± 0.15 at.% Al, 5.01 ± 0.07 at.% Zr, 18.96 ± 0.13 at.% Sc and 2.75 ± 0.05 at.% Er.

3.3. Isothermal aging at 400 °C

The precipitation behavior of the alloys during isothermal aging at 400 °C for aging times from 0.5 min to 256 days, as monitored by Vickers microhardness and electrical conductivity, is displayed in Fig. 5. The Vickers microhardness of Al–0.06 Zr–0.06 Sc does not increase significantly over the full range of aging times, which is surprising given the strengths achieved by isochronal aging (see Fig. 2) and in earlier research [31]. The electrical conductivity of Al–0.06 Zr–0.06 Sc remains unchanged over the first 0.5 h of aging at 400 °C, before increasing steadily over the subsequent 64 days. Small strengths in dilute Al–Sc alloys with Sc concentrations of 0.06–0.07 at.% have been observed previously to be a result of inadequate solute supersaturation, resulting in a small number density of larger precipitates, which do not strengthen the material

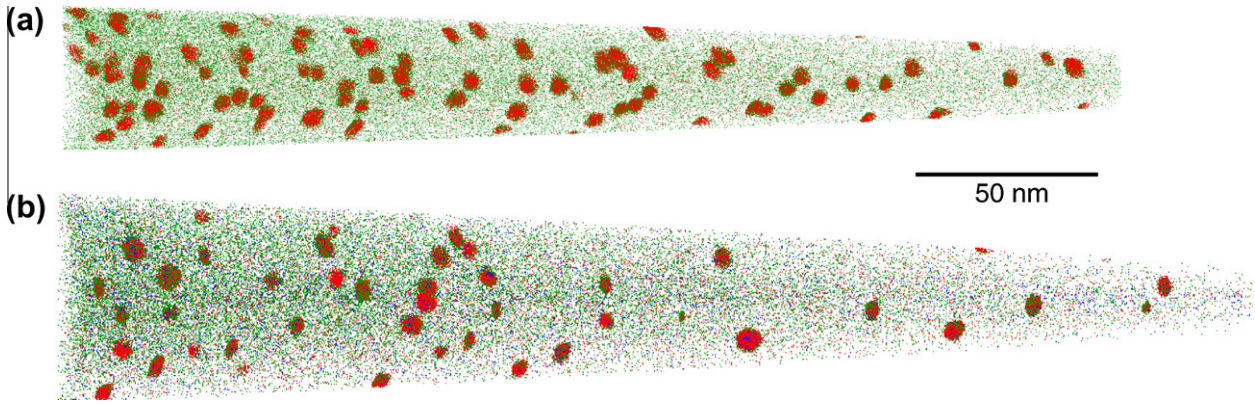

Fig. 3. Atom-probe tomographic reconstructions of samples aged isochronally in 25 °C h^{-1} stages to 450 °C, displaying precipitates for (a) Al–0.06 Zr–0.06 Sc and (b) Al–0.06 Zr–0.04 Sc–0.02 Er. Sc atoms are displayed in red, Zr atoms are in green, Er atoms are in blue, and Al atoms are omitted for clarity. (For interpretation of the references to colour in this figure legend, the reader is referred to the web version of this article.)

Table 3
Precipitate number density, N_v, mean radius, $\langle R \rangle$, volume fraction, ϕ, and Vickers microhardness, HV, for alloys aged isochronally to 450 °C (in stages of 25 °C h^{-1}), or isothermally at 400 °C.

Alloy	N_v ($\times 10^{22}$ m^{-3})	$\langle R \rangle$ (nm)	ϕ (%)	HV (MPa)
Al–0.06 Zr–0.06 Sc (isochronal to 450 °C)	2.1 ± 0.2	3.1 ± 0.4	0.251 ± 0.002	597 ± 12
Al–0.06 Zr–0.04 Sc–0.02 Er (isochronal to 450 °C)	0.86 ± 0.15	3.4 ± 0.6	0.157 ± 0.003	463 ± 16
Al–0.06 Zr–0.04 Sc–0.02 Er (0.5 h isothermal at 400 °C)	0.54 ± 0.17	3.7 ± 0.3	0.144 ± 0.006	414 ± 11
Al–0.06 Zr–0.04 Sc–0.02 Er (64 days isothermal at 400 °C)	0.61 ± 0.19	3.8 ± 0.4	0.207 ± 0.007	448 ± 21

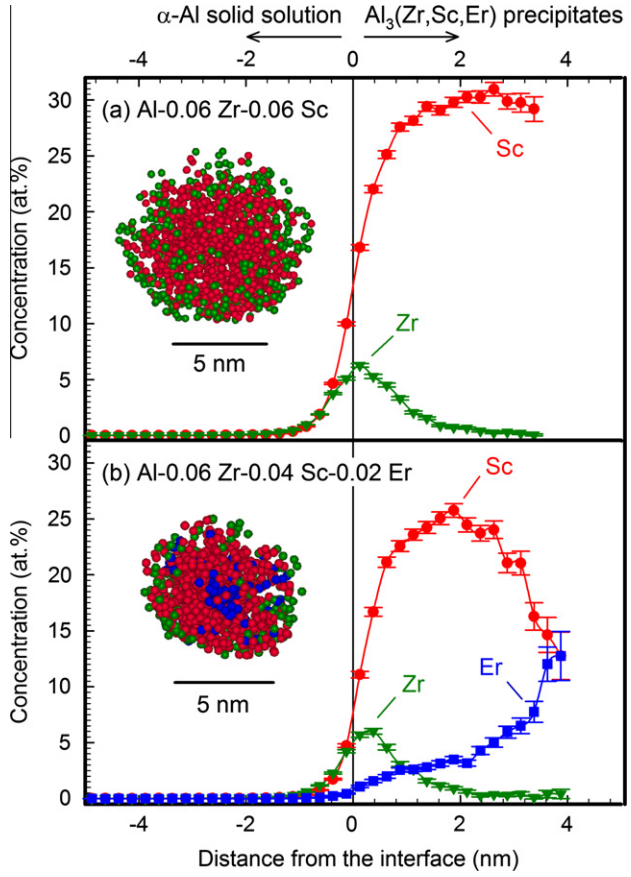

Fig. 4. Concentration profiles across the matrix/precipitate interface following isochronal aging to 450 °C in stages of 25 °C h^{-1} for (a) Al–0.06 Zr–0.06 Sc, exhibiting Zr enrichment near the interface, and (b) Al–0.06 Zr–0.04 Sc–0.02 Er, further exhibiting Er enrichment at the precipitate core. The inset images in (a and b) are APT reconstructions of a representative precipitate from each alloy. Sc atoms are shown in red, Zr atoms are in green, Er atoms are in blue, and the Al atoms are omitted for clarity. (For interpretation of the references to colour in this figure legend, the reader is referred to the web version of this article.)

significantly [2,14]. The size and the morphology of the precipitates in Al–0.06 Zr–0.06 Sc aged for 24 h at 400 °C are presented in the TEM micrograph shown in Fig. 6. The precipitates, which have large radii, of the order of 50 nm, have a non-equilibrium lobed-cuboidal morphology. This morphology is due to growth instabilities that accommodate the anisotropy of the elastic constants of the matrix and the precipitates [2,14] (Section 4.3).

The microhardness values of the two Er-containing alloys during isothermal aging at 400 °C are comparable over the full range of aging times. Both alloys exhibit a microhardness increase after 0.5 min, with a concomitant increase in the electrical conductivity. After 0.5 h of aging, the microhardness values of Al–0.06 Zr–0.05 Sc–0.01 Er and Al–0.06 Zr–0.04 Sc–0.02 Er are 422 ± 12 and 414 ± 11 MPa, respectively. This is in dramatic contrast to the Er-free alloy, whose microhardness does not increase beyond the homogenized value of 199 ± 14 MPa after 0.5 h, and achieves a peak microhardness of only 243 ± 3 MPa after 8 days at 400 °C. By contrast, the microhardness of Al–0.06 Zr–0.05 Sc–0.01 Er peaks at a value of 461 ± 15 MPa after 2 days, and diminishes slightly to 438 ± 21 MPa after 64 days of aging at 400 °C. The Al–0.06 Zr–0.04 Sc–0.02 Er alloy has a maximum microhardness of 451 ± 11 MPa after 1 day of aging, and has the same microhardness, within uncertainty, of 448 ± 21 MPa after 64 days at 400 °C. The microhardness values of the Er-containing alloys decrease for aging times of 128 and 256 days due to precipitate coarsening. The electrical conductivities of the Er-containing alloys increase steadily over the first 1–2 days, as precipitation proceeds. Between 2 and 64 days, the electrical conductivities of both alloys achieve plateaus, indicating that the majority of the available solute has precipitated out of solution. The electrical conductivities of the alloys increase slightly after 128 and 256 days of aging, as the alloys continue to slowly approach equilibrium.

The nanostructures of Al–0.06 Zr–0.04 Sc–0.02 Er aged isothermally for 0.5 h and 64 days at 400 °C are compared employing LEAP tomography in Fig. 7. From the LEAP tomographic images, and the associated concentration profiles (Fig. 8), it is clear that the precipitates consist of an Er-enriched core surrounded by a Sc-enriched shell after 0.5 h of aging. After 0.5 h of aging, Al–0.06 Zr–0.04 Sc–0.02 Er has a number density of precipitates of 5.4 ± 1.7 × 10^{21} m^{-3}, with an average radius of 3.7 ± 0.3 nm, and a volume fraction of 0.144 ± 0.006% (Table 3). The number density of 6.1 ± 1.9 × 10^{21} m^{-3} and the radius of 3.8 ± 0.4 nm are unchanged, within uncertainty, after 64 days at 400 °C, although the volume fraction increases to 0.207 ± 0.007%.

After 0.5 h of aging at 400 °C, the precipitates in Al–0.06 Zr–0.04 Sc–0.02 Er consist of an Er-enriched core surrounded by a Sc-enriched shell structure with an average precipitate composition of 73.02 ± 0.20 at.% Al, 0.64 ± 0.04 at.% Zr, 22.25 ± 0.19 at.% Sc and 4.08 ± 0.09 at.% Er at.% (Table 4). The average precipitate composition after 64 days at 400 °C, 70.46 ± 0.22 at.% Al, 6.55 ±

Table 4
Compositions of the precipitates and matrix in alloys aged isochronally to 450 °C (in stages of 25 °C h^{-1}) or isothermally at 400 °C.

Alloy	Precipitate composition (at.%)				Matrix composition (at. ppm)		
	Al	Zr	Sc	Er	Zr	Sc	Er
Al–0.06 Zr–0.06 Sc (isochronal to 450 °C)	71.95 ± 0.10	5.42 ± 0.05	22.63 ± 0.09	–	127 ± 5	159 ± 4	–
Al–0.06 Zr–0.04 Sc–0.02 Er (isochronal to 450 °C)	73.27 ± 0.15	5.01 ± 0.07	18.96 ± 0.13	2.75 ± 0.05	133 ± 9	168 ± 7	9 ± 4
Al–0.06 Zr–0.04 Sc–0.02 Er (0.5 h isothermal at 400 °C)	73.02 ± 0.20	0.64 ± 0.04	22.25 ± 0.19	4.08 ± 0.09	167 ± 14	70 ± 6	0 ± 8
Al–0.06 Zr–0.04 Sc–0.02 Er (64 days isothermal at 400 °C)	70.46 ± 0.22	6.55 ± 0.12	19.75 ± 0.19	3.24 ± 0.09	35 ± 15	25 ± 6	13 ± 9

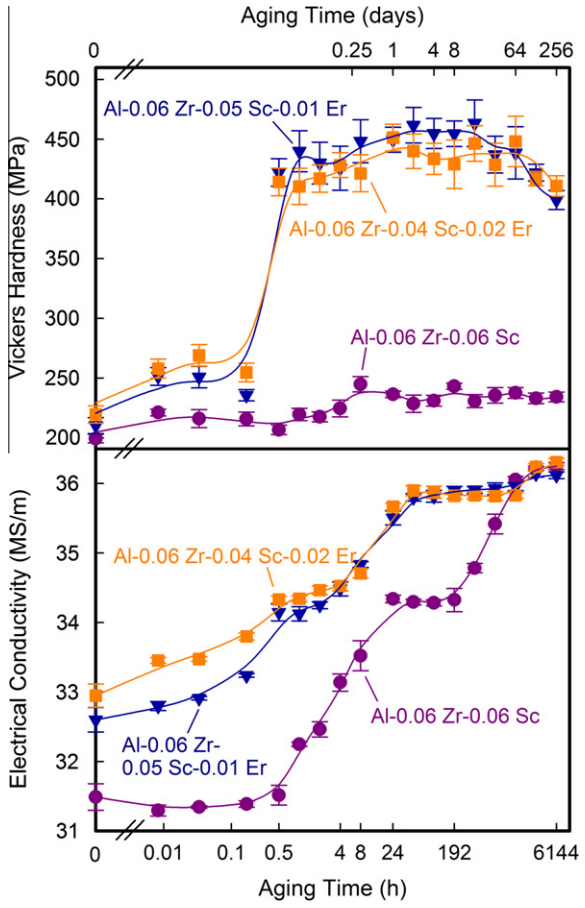

Fig. 5. Evolution of the Vickers microhardness and electrical conductivity during isothermal aging at 400 °C for Al–0.06 Zr–0.06 Sc, Al–0.06 Zr–0.05 Sc–0.01 Er and Al–0.06 Zr–0.04 Sc–0.02 Er.

0.12 at.% Zr, 19.75 ± 0.19 at.% Sc, 3.24 ± 0.09 at.% Er, reflects the precipitation of the Zr-enriched outer shell, which renders the precipitates coarsening resistant. The matrix is depleted of Sc and Zr as precipitation proceeds, as evidenced by decreases in the Zr concentration from 167 ± 14 to 35 ± 15 at. ppm, and in Sc from 70 ± 6 to 25 ± 6 at. ppm between 0.5 h and 64 days.

The precipitation behavior of the three alloys exhibits three distinct stages of development at 400 °C (Fig. 5). In the Er-containing alloys, a short incubation period of 0.5 min is followed by a rapid increase in the microhardness and electrical conductivity over the first hour, associated with the precipitation of Er and Sc (Fig. 7a), which is followed by a slower increase in conductivity due to

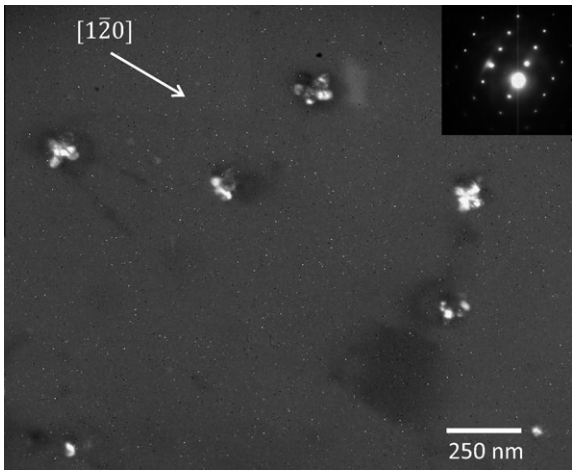

Fig. 6. Superlattice dark-field transmission electron microscopy image of $Al_3(Sc,Zr)$ ($L1_2$) precipitates in Al–0.06 Zr–0.06 Sc aged isothermally at 400 °C for 24 h imaged along the [2 1 0] zone axis using the 1 $\bar{2}$ 0 reflection.

the precipitation of Zr (Fig. 7b). In Al–0.06 Zr–0.06 Sc, the incubation period of 0.5 h is followed by a rapid increase in the electrical conductivity from 0.5 to 24 h as Sc precipitates from solution, followed by a slow second increase in the conductivity due to precipitation of Zr.

3.4. Two-stage (24 h at 300 °C + 400 °C) isothermal aging

A two-stage heat treatment was performed: (i) to improve the microhardness of Al–0.06 Zr–0.06 Sc at 400 °C; and (ii) to optimize the nanostructure, and hence the microhardness, of the Er-containing alloys. The first stage of the heat treatment was performed at 300 °C for 24 h—an aging treatment that has been shown to produce peak microhardness in Al–0.06 at.% Sc alloys with and without 0.02 at.% RE additions [2,23,24,34]. The objective of this first stage is to precipitate the Er and Sc atoms from solution at a temperature as low as practical, maximizing the solute supersaturation, and hence the number density of precipitates. Zr is essentially immobile in Al at 300 °C over a period of 24 h, with a root-mean-square (RMS) diffusion distance, $\sqrt{4Dt}$, of 1.5 nm, as compared to RMS diffusion distances of 56 and 372 ± 186 nm for Sc and Er, respectively, where D is the diffusivity: the values of D are given in Table 2. The second stage of the heat treatment, designed to precipitate Zr, was performed at 400 °C for aging times ranging from 0.5 h to 64 days. At 400 °C, the Zr RMS diffusion distance after 24 h is 64 nm, comparable to the Sc RMS diffusion distance of

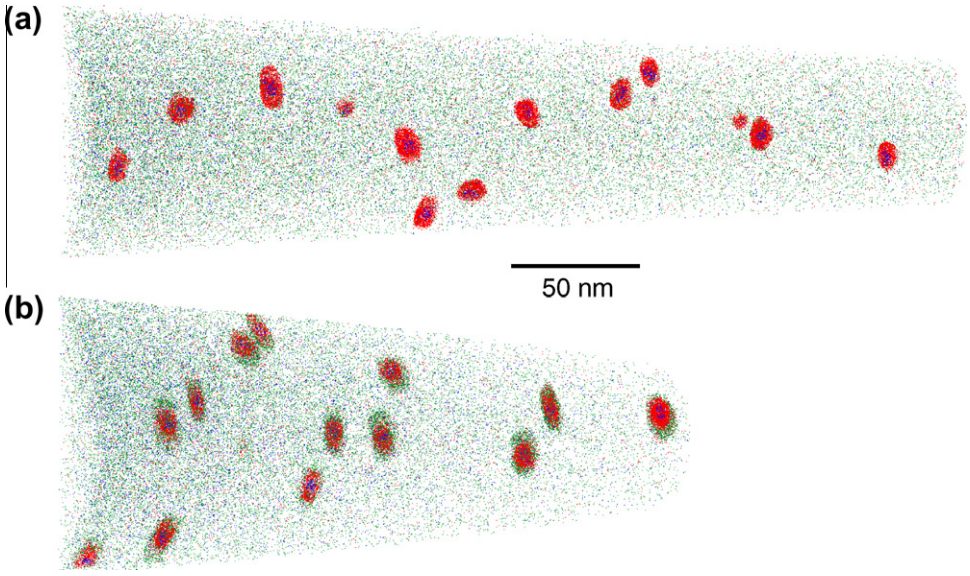

Fig. 7. Atom-probe tomographic reconstructions of Al–0.06 Zr–0.04 Sc–0.02 Er samples aged isothermally at 400 °C for (a) 0.5 h, with core/shell precipitates and (b) 64 days, with core/double-shell precipitates. Sc atoms are shown in red, Zr atoms are green, Er atoms are in blue, and the Al atoms are omitted for clarity. (For interpretation of the references to colour in this figure legend, the reader is referred to the web version of this article.)

56 nm in 24 h at 300 °C. The precipitation response during the second stage, as monitored by the Vickers microhardness and electrical conductivity, is displayed in Fig. 9.

The microhardness of Al–0.06 Zr–0.06 Sc following the two-stage 300/400 °C heat treatment (Fig. 9), is significantly improved compared to the values measured for the single isothermal aging at 400 °C (Fig. 5). After 24 h at 300 °C, the microhardness of Al–0.06 Zr–0.06 Sc is 523 ± 7 MPa, compared to 236 ± 3 MPa after 24 h at 400 °C (Fig. 5). The aging treatment at 300 °C provides sufficient solute supersaturation to precipitate a significant number density (10^{21}–10^{22} m^{-3}), of spheroidal precipitates, such as those obtained during isochronal aging (Fig. 3). Following a second heat treatment of 8 h at 400 °C, the microhardness achieves a maximum value of 561 ± 14 MPa, and decreases only slightly to 533 ± 31 MPa after 64 days at 400 °C.

The Er-containing alloys achieve peak microhardness after 8 h of aging at 400 °C, with values of 507 ± 11 and 489 ± 11 MPa for Al–0.06 Zr–0.05 Sc–0.01 Er and Al–0.06 Zr–0.04 Sc–0.02 Er, respectively. These peak values are larger than those achieved in single-stage isothermal aging at 400 °C (461 ± 15 and 451 ± 11 MPa). The Er-containing alloys that underwent two-stage aging experience only a slight decrease in microhardness after 64 days at 400 °C, from 507 ± 11 to 464 ± 23 MPa for Al–0.06 Zr–0.05 Sc–0.01 Er, and from 489 ± 11 to 458 ± 19 MPa for Al–0.06 Zr–0.04 Sc–0.02 Er.

4. Discussion

4.1. Origins and stability of the core/double-shell structure

Core/double-shell precipitates were previously found in an Al–6.3 Li–0.069 Sc–0.018 Yb alloy aged in two steps from the homogenized state: (i) at 325 °C for 8 h; and (ii) at 170 °C for 1 week [54,55]. The precipitate nanostructure was formed by selecting alloying elements with disparate solubilities and diffusivities in Al, i.e., $D_{Li} > D_{Yb} > D_{Sc}$. The 325 °C aging treatment produced precipitates with a core enriched in the faster-diffusing Yb, and a shell enriched in the slower-diffusing Sc. Lithium replaced some of the Yb and Sc in the core/shell precipitates, though most of the Li remained in solution due to its high solubility in Al at 325 °C. The second aging treatment at 170 °C resulted in heterogeneous precipitation of the highly mobile Li as a second shell with nearly stoichiometric Al_3Li ($L1_2$) on some of the original core/shell precipitates. The strategy employed in the Al–Li–Sc–Yb system of precipitating Yb and Sc at a higher temperature, and then Li at a lower temperature, differs from that in the present work, where a core/double-shell structure was formed during (i) isothermal aging at 400 °C or (ii) during two-stage aging (24 h at 300 °C + 400 °C) where Er and Sc precipitate at 300 °C and Zr precipitates at 400 °C.

A two-stage aging procedure was used in previous research to form Al_3Li ($L1_2$) shells at 190 °C on $Al_3(Zr_xSc_{1-x})$ ($L1_2$) cores nucleated at 450 °C in an Al–6.3 Li–0.36 Sc–0.13 Zr at.% [56]. The resulting nanostructure exhibited Zr segregation between the Sc-enriched core and the outer Li-enriched shell, which was too weak to qualify as an independent shell. In other research, isothermal aging at 300 °C in Al–0.02 Zr–0.06 Sc–0.02 Yb and Al–0.005 Zr–0.06 Sc–0.02 Yb at.% alloys resulted in the precipitation of a Sc- and Yb-enriched core with a uniform distribution of both elements, with Zr segregation outside of the core that did not qualify as a shell [27]. The addition of Zr to the Al–Sc–Yb system decelerated the precipitation of Yb, resulting in simultaneous precipitation of Sc and Yb, followed by the gradual segregation of Zr to the outside of the precipitates.

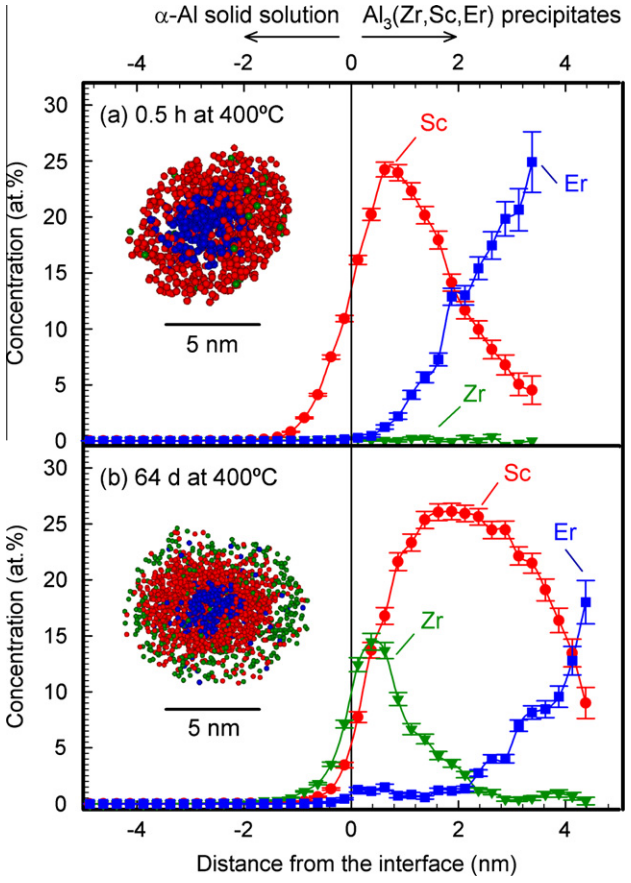

Fig. 8. Concentration profiles across the matrix/precipitate interface for Al–0.06 Zr–0.04 Sc–0.02 Er samples aged isothermally at 400 °C for (a) 0.5 h, with precipitates showing an Er-enriched core and a Sc-rich shell and (b) 64 days, with precipitates showing an Er-enriched core, an inner Sc-enriched shell and an outer Zr-enriched shell. The inset images in (a and b) are APT reconstructions of a representative precipitate from each alloy. Sc atoms are displayed in red, Zr atoms are in green, Er atoms are in blue, and the Al atoms are omitted for clarity. (For interpretation of the references to colour in this figure legend, the reader is referred to the web version of this article.)

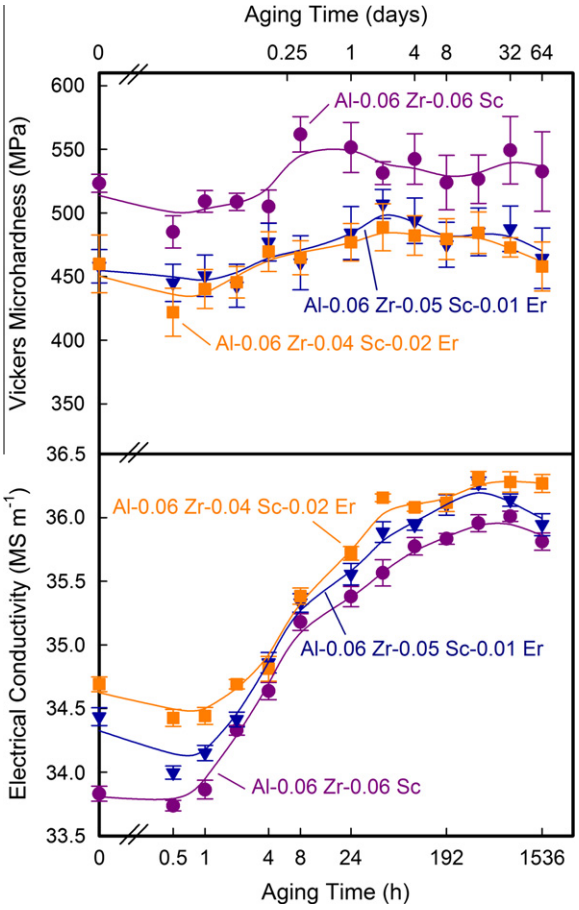

Fig. 9. Temporal evolution of the Vickers microhardness and electrical conductivity during isothermal aging at 400 °C for Al–0.06 Zr–0.06 Sc, Al–0.06 Zr–0.05 Sc–0.01 Er and Al–0.06 Zr–0.04 Sc–0.02 Er previously aged 24 h at 300 °C.

In the alloys studied here, where $D_{Er} > D_{Sc} > D_{Zr}$, the core/double-shell structure is anticipated, given the relative magnitudes of the solute diffusivities. The stability of this structure, however, is determined by thermodynamics, in particular the total interfacial energy between the core, shells and matrix, the reduction of which provides the driving force for coarsening. Recent first-principles results have shown that the total interfacial energy of the Al–Zr–Sc–Er system is minimized by the formation of the core/double-shell structure [57]. Of the three simulated {1 0 0} outer-shell interfacial structures, α-Al/Al_3Zr ($L1_2$), α-Al/Al_3Sc ($L1_2$) and α-Al/Al_3Er ($L1_2$), the former has the lowest interfacial energy, 128 mJ m^{-2}, while the latter two have energies of 171 and 312 mJ m^{-2}, respectively. As such, the outer shell is enriched in Zr (Figs. 4 and 8). The inner shell is enriched in Sc because Al_3Zr ($L1_2$)/Al_3Sc ($L1_2$) has a lower interfacial energy of 115 mJ m^{-2} than that of 234 mJ m^{-2} for Al_3Zr ($L1_2$)/Al_3Er ($L1_2$). The core/double-shell structure is therefore favored kinetically and thermodynamically, translating into coarsening resistance for 64 days at 400 °C or 0.72T_m (T_m is the absolute melting point of Al, 933.52 K).

4.2. Role of Er in precipitation kinetics

The hardening responses of the isochronally and isothermally aged alloys demonstrate that the addition of Er alters the kinetic pathways that lead to phase decomposition in Al–Zr–Sc. The addition of Er decreases the temperature at which precipitation commences in isochronal aging from 300 to 200 °C (Fig. 2), and decreases the time for precipitation initiation in isothermal aging at 400 °C, from 0.5 h to 0.5 min (Fig. 5). The addition of Er also alters the dimensions and morphology of the precipitates formed during aging at 400 °C, from lobed-cuboids with dimensions on the order of 100 nm (Fig. 6) to spheroids with radii on the order of 3–4 nm (Fig. 7). These changes are particularly remarkable given that only 46 ± 2 at. ppm Er is available in the matrix to participate in strengthening precipitation in these alloys (see Section 3.1).

The addition of Er decreases the incubation time for precipitation during isothermal aging and decreases the

temperature at which precipitation commences in isochronal aging. Similar effects have been observed in prior studies of Al–Sc alloys with the RE element additions of Er, Yb, Gd, Ho, Lu, Tm, Tb [23–25,53,58]. Within the framework of classical nucleation theory [59–63], and following the analysis in Ref. [24], these results are consistent with: (i) a smaller α-Al/precipitate interfacial free-energy, $\gamma^{\alpha/\alpha'}$; (ii) a larger excess chemical free-energy and/or a smaller coherent elastic strain energy; and (iii) a larger diffusivity of the precipitating solute species.

The thermodynamic and kinetic data available for these alloys is limited, so classical nucleation theory can only provide a qualitative understanding of the role of Er in the acceleration of the precipitation kinetics. In a recent study of the coarsening kinetics of an Al–0.06 Sc–0.02 Er alloy at 300 °C, which formed an Er-enriched core/Sc-enriched shell structure similar to the one in Fig. 7a, the α-Al/$Al_3(Sc_x,Er_{1-x})$ ($L1_2$) interfacial free energy was determined to be 0.5 ± 0.2 J m^{-2} [21]. This value is larger than that in the binary Al–Sc system, for which values of 0.14–0.20 J m^{-2} [64–66] were calculated for α-Al/Al_3Sc ($L1_2$), and values of ~0.22 J m^{-2} were measured from coarsening and electrical resistivity data [67]. We note that the α-Al/Al_3Er ($L1_2$) interfacial free energy was calculated to be 0.4 ± 0.2 J m^{-2} in an Al–0.045 Er at.% alloy aged at 300 °C [25]. Thus, if the incubation time is determined primarily by the interfacial free energy, the Er-containing alloys studied would have longer incubation periods than Al–0.06 Zr–0.06 Sc, whereas the opposite is observed. Thus, a change in the interfacial free energy due to the addition of Er is not responsible for the accelerated precipitation kinetics observed in the present Al–Zr–Sc–Er alloys.

The chemical formation energies of Al_3Sc ($L1_2$) and Al_3Er ($L1_2$) are comparable, with values of −43.5 to −50 kJ mol^{-1} [65,68–71] and −40 kJ mol^{-1} [72], respectively. The chemical driving force of Al–0.06 Zr–0.04 Sc–0.02 Er, however, is smaller than that of Al–0.06 Zr–0.06 Sc, since the solute content in the former is lower because only 0.0046 ± 0.0004 at.% Er is available for precipitation (Table 1). The elastic strain energy is expected to be larger in the Er-containing alloys, given that the lattice mismatch parameter δ with Al is larger for Al_3Er ($L1_2$) ($\delta = +4.08\%$ at ambient temperature [29]) than for Al_3Sc ($L1_2$) ($\delta = +1.32\%$ at ambient temperature [73]). As such, the total change in free energy associated with nucleation is expected to be larger for Al–0.06 Zr–0.06 Sc than for Al–0.06 Zr–0.04 Sc–0.02 Er, leading to shorter incubation times, though the opposite is observed. Thus, a change in the total free energy upon nucleation due to the addition of Er is not responsible for the acceleration in precipitation.

Given that the total free energy for nucleation is smaller, and the interfacial energy larger, in the Er-containing alloys, the shorter incubation times and precipitation at lower temperatures must be due exclusively to an increase in the diffusivity of the precipitating species. Indeed, the diffusivity of Er, $D_{Er} = 4 \pm 2 \times 10^{-19}$ m^2 s^{-1}, as determined from Al_3Er ($L1_2$) coarsening experiments in an Al–0.045 at.% Er alloy at 300 °C [25], is significantly larger than that of Sc, $D_{Sc} = 9.1 \times 10^{-20}$ m^2 s^{-1} at 300 °C [52]. No diffusion data is available for Er in Al at 400 °C, though the diffusivity of Er in Al likely remains higher than that of Sc at 400 °C.

4.3. Precipitate morphology

The equilibrium morphology of Al_3Sc ($L1_2$) precipitates that nucleate and grow from a supersaturated Al–Sc solid solution was determined to be a great rhombicuboctahedron, with 8 {1 1 1}, 12 {1 1 0} and 6 {1 0 0} facets [2,65]. The addition of Zr in an Al–0.09 Sc–0.047 Zr alloy aged at 300 °C did not alter the morphology significantly, as the precipitates were found to have facets parallel to the {1 0 0} and {1 1 0} planes [13,14]. Spheroidal precipitates were, however, found in the Al–0.09 Sc–0.047 Zr alloy aged at 350 °C [13,14]. The formation of an outer Zr-enriched shell at 350 °C decreased the value of the α-Al/$Al_3(Zr_xSc_{1-x})$ {1 1 1} and {1 1 0} interfacial free energies to values closer to that of the {1 0 0} facets [13,14], favoring the formation of spheroidal precipitates. As such, a spheroidal equilibrium precipitate morphology (see Figs. 3 and 7) is expected in this research due to precipitation of the Zr-enriched outer shell (Figs. 4 and 8).

The non-equilibrium lobed-cuboidal precipitate morphology (Fig. 6) has been observed previously in dilute Al–Sc alloys to be a result of an inadequate solute supersaturation [2,14]. Marquis et al. surmised that at low supersaturations, the number density of precipitates is sufficiently small so that precipitate growth occurs in a supersaturated matrix before the precipitate diffusion fields commence overlapping [2]. This results in a morphology that is determined by the growth conditions, not the equilibrium thermodynamic conditions. The specific lobed cuboidal morphology we observed was predicted by Lee for $L1_2$ precipitates in Ni-based superalloys, employing the discrete atom method [74]. Lee determined that the lobed cuboidal morphology occurs when the elastically soft direction of the matrix is parallel to the hard direction of the precipitate. In the Al–Sc system, the elastic strain energy is relaxed by elongation of the precipitates along their elastically soft ⟨1 1 0⟩ directions, while remaining truncated in the elastically soft ⟨1 0 0⟩ directions of the matrix [75]. The anisotropy of the elastic constants of the matrix and the precipitates leads to a 2- or 4-fold symmetrical shape of precipitates, with possible splitting parallel to the {1 0 0} planes, as observed here and in prior work on low-supersaturation Al–Sc alloys [2,14].

The replacement of 200 at. ppm Sc with 46 ± 2 at. ppm Er in Al–0.06 Zr–0.06 Sc results in a radical change in the precipitate morphology, number density and average radius for alloys aged at 400 °C (Figs. 6 and 7). The acceleration in the precipitation kinetics due to the addition of Er leads to the nucleation of a larger number density of smaller spheroidal precipitates after 0.5 h at 400 °C

Table 5
Experimental (ΔHV/3) and calculated strength increments (Eqs. (1A)–(4A)). For all four peak-aged alloys, the Orowan bypass strengthening mechanism (Eq. (4A)) is predicted to be controlling.

Alloy	ΔHV/3 (MPa)	$\Delta\sigma_{ord}$ (MPa) (Eq. (1A))	$\Delta\sigma_{coh}+\Delta\sigma_{mod}$ (MPa) (Eqs. (2A) and (3A))	$\Delta\sigma_{Or}$ (MPa) (Eq. (4A))
Al–0.06 Zr–0.06 Sc (isochronal to 450 °C)	133 ± 4	118 ± 1	165 ± 5	112 ± 20
Al–0.06 Zr–0.04 Sc–0.02 Er (isochronal to 450 °C)	81 ± 6	93 ± 1	135 ± 7	82 ± 24
Al–0.06 Zr–0.04 Sc–0.02 Er (0.5 h isothermal at 400 °C)	72 ± 4	89 ± 2	133 ± 3	74 ± 9
Al–0.06 Zr–0.04 Sc–0.02 Er (64 days isothermal at 400 °C)	76 ± 7	104 ± 2	156 ± 4	86 ± 13

(Fig. 7a), which experience minimal growth and coarsening as aging proceeds (Fig. 7b and Table 3). In Al–0.06 Zr–0.06 Sc, such a structure is achieved during isochronal aging (Fig. 3a), where nucleation begins at ~300 °C (Fig. 2). During isothermal aging at 400 °C, the Er-free alloy forms a small number density of precipitates due to the lower supersaturation at a higher temperature, and the precipitates adopt the lobed-cuboidal morphology as they grow.

4.4. Compositional evolution

The temporal evolution of the compositions of the matrix and precipitate phases in Al–0.06 Zr–0.04 Sc–0.02 Er at 400 °C provides insight into the kinetic pathways of precipitation in the Al–Zr–Sc–Er alloy system. The matrix is depleted of Sc and Zr between 0.5 h and 64 days as evidenced by decreases in the Zr concentration from 167 ± 14 to 35 ± 15 at. ppm, and in Sc from 70 ± 6 to 25 ± 6 at. ppm. The change in the Er concentration in the matrix from 0 ± 8 and 13 ± 9 at. ppm Er is statistically insignificant, meaning that all of the Er has precipitated out of solution after 0.5 h—another indication of the rapid precipitation kinetics of Er in these alloys. The matrix composition of Al–0.06 Zr–0.04 Sc–0.02 Er after 64 days at 400 °C of 35 ± 15 at. ppm Zr, 25 ± 6 at. ppm Sc and 13 ± 9 at. ppm Er is a measured upper bound for the matrix solubility at 400 °C. The total measured matrix solute solubility of 73 ± 18 at. ppm is comparable to the solubility of 100 at. ppm Sc in Al–Sc [73,76], and significantly larger than that of 5 at. ppm Zr in Al–Zr [77], or of ~0 at. ppm Er in binary Al–Er [78]—all at 400 °C. The average precipitate composition after 64 days at 400 °C of 70.46 ± 0.22 at.% Al, 6.55 ± 0.12 at.% Zr, 19.75 ± 0.19 at.% Sc, 3.24 ± 0.09 at.% Er demonstrates that Zr and Er are effective substitutes for Sc in the precipitates, accounting for one-third (33 ± 1%) of the total solute concentration of the precipitates.

4.5. Strengthening mechanisms

There is no evidence of a loss of precipitate coherency, such as rapid over-aging, in the peak-aged alloys, so models for ambient-temperature strengthening by coherent precipitates apply. The coherency of Al_3Sc ($L1_2$) precipitates in binary alloys is maintained for radii ranging from 14 to 25 nm at elevated temperatures [2,5,67,79–83]. The addition of Er, however, which increases the lattice parameter misfit of $Al_3(Sc,Er)$ ($L1_2$), is anticipated to decrease the radius at which coherency is lost, though coherency was maintained to a radius of 8 ± 2 nm in an Al–0.06 Sc–0.02 Er alloy aged at 300 °C for 64 days [21]. By contrast, the Zr shell that surrounds the precipitates in the alloys studied increases the radius at which coherency is lost by decreasing the lattice parameter misfit [13,84,85]. As such, coherency loss is very improbable in the alloys we studied, where precipitate radii are of the order of 3–4 nm.

To determine the operating precipitate-strengthening mechanisms, the strength increments for order strengthening ($\Delta\sigma_{ord}$), coherency and modulus strengthening ($\Delta\sigma_{coh}+\Delta\sigma_{mod}$), or strengthening by the Orowan bypass mechanism ($\Delta\sigma_{Or}$), are calculated employing the same methodology as in Refs. [3,24,32,34] and are listed in Table 5: the equations are given in the Appendix. The predicted strengthening increments are compared to the measured strength increment, estimated as ΔHV/3 [86], where ΔHV is the increase in microhardness from the as-quenched state to the aged state. Following the research referenced above, we take the strengthening increment due to precipitate shearing as the larger of (a) the sum of modulus strengthening and coherency strengthening, or (b) the order strengthening. This is because the mechanisms in (a and b) occur sequentially as dislocations move towards the matrix/precipitate interface and shear the precipitates. Shearing and Orowan bypass occur, however, in parallel, thus strengthening is dictated by the mechanism that requires the smallest stress. The critical radius at which the deformation mechanism changes from precipitate shearing to an Orowan bypass mechanism in the Al–Sc system is 1.5–2.0 nm in an Al–0.18 at.% Sc alloy [3,87]. Accordingly, for the four aging conditions we studied, with average precipitate radii ranging from 3.1 to 3.8 nm, the Orowan bypass mechanism is predicted to be operative, as confirmed by numerical results (Table 5). This table also shows that there is good agreement between the measured and predicted Orowan strength increments, as also reported for Al–0.06 at.% Sc alloys with and without dilute additions of Zr, Ti, Gd, Tb, Dy, Ho, Er, Tm, Yb and Lu [3,23,24,34,53,58,88].

5. Conclusions

The effect of substituting Er for Sc in an Al–0.06 Zr–0.06 Sc at.% alloy was studied with the goal of developing Al alloys to replace some cast iron and titanium alloy components subjected to low stresses in existing automotive and aerospace applications at temperatures up to 400 °C. The conclusions from this work are now summarized:

- Coherent, spheroidal, $L1_2$-ordered precipitates with a nanostructure consisting of an Er-enriched core surrounded by a Sc-enriched inner shell and a Zr-enriched outer shell were formed. This core/double-shell structure is formed upon aging as solute elements precipitate sequentially according to their diffusivities, where $D_{Er} > D_{Sc} > D_{Zr}$. The core/double-shell structure remains coarsening resistant for at least 64 days at 400 °C.
- The effective Zr and Er concentrations of the alloys were diminished to 200–300 at. ppm Zr and 46 ± 2 at. ppm Er, as measured by APT, due to incomplete dissolution of the Al–Zr master alloy, and the formation of primary Al_3Er ($L1_2$) precipitates during solidification and homogenization.
- Zr and Er are effective replacements for Sc, accounting for $33 \pm 1\%$ of the total precipitate solute content in Al–0.06 Zr–0.04 Sc–0.02 Er aged at 400 °C for 64 days. The measured precipitate composition for this aging condition is 70.46 ± 0.22 at.% Al, 6.55 ± 0.12 at.% Zr, 19.75 ± 0.19 at.% Sc, 3.24 ± 0.09 at.% Er. The matrix solute composition after 64 days at 400 °C is 35 ± 15 at. ppm Zr, 25 ± 6 at. ppm Sc and 13 ± 9 at. ppm Er, providing an upper bound for the matrix solute solubility at 400 °C.
- In the absence of Er, a low number density of non-equilibrium lobed-cuboidal precipitates is formed during isothermal aging at 400 °C, resulting in a peak microhardness of only 243 ± 3 MPa after 8 days compared to the homogenized value of 199 ± 14 MPa. The lobed-cuboidal morphology is a result of slow nucleation kinetics, and develops to accommodate the anisotropy of the elastic constants of the matrix and the precipitates.
- The addition of Er leads to precipitate nucleation during isochronal aging at 200 °C, whereas precipitation is delayed until 300 °C in the Er-free alloy. Er also decreases the incubation time for precipitation during isothermal aging at 400 °C from 0.5 h to 0.5 min. This acceleration of the precipitation kinetics is because $D_{Er} > D_{Sc}$ in Al.
- In the peak-strengthened Al–Zr–Sc and Al–Zr–Sc–Er alloys studied, where the average precipitate radii range from 3.1 to 3.8 nm, the Orowan bypass mechanism is predicted to be operative, with good agreement between the measured and predicted strengthening increment.
- A two-stage aging treatment of 24 h at 300 °C, followed by further aging at 400 °C, significantly improves the microhardness of Al–0.06 Zr–0.06 Sc during subsequent isothermal aging at 400 °C. After 24 h at 300 °C, the microhardness of Al–0.06 Zr–0.06 Sc is 523 ± 7 MPa, compared to 236 ± 3 MPa after 24 h at 400 °C. The aging treatment at 300 °C provides sufficient solute supersaturation to precipitate a significant number density (10^{21}–10^{22} m^{-3}) of nanoscale spheroidal precipitates, eliminating the lobed-cuboidal precipitate morphology.

Acknowledgements

This research was sponsored by the Ford-Boeing-Northwestern University Alliance (81132882). Atom-probe tomographic measurements were performed at the Northwestern University Center for Atom-probe Tomography (NUCAPT). The LEAP tomography system was purchased and upgraded with funding from NSF-MRI (DMR-0420532) and ONR-DURIP (N00014-0400798, N00014-0610539, and N00014-0910781) Grants. We thank M. Krug (NU) for his assistance with casting, TEM and many useful discussions, A. Hunter (NU) and M. Diaz (NU) for their assistance with SEM and Dr. D. Isheim for his assistance with LEAP tomography. We thank Dr. K. Knipling (Naval Research Laboratory) for his suggestions regarding casting and heat treatment, Prof. C. Wolverton (NU) and Dr. Z. Mao (NU) for sharing the results of their first-principles calculations, and Dr. J. Boileau (Ford), Dr. B. Ghaffari (Ford) and Mr. C. Huskamp (Boeing) for numerous useful discussions.

Appendix A

The strength increments for order strengthening ($\Delta\sigma_{ord}$), coherency and modulus strengthening ($\Delta\sigma_{coh} + \Delta\sigma_{mod}$), and strengthening by the Orowan bypass mechanism ($\Delta\sigma_{Or}$), are calculated employing the methodology described in Refs. [3,89,90]. First, the contribution to the yield strength from order strengthening is given by:

$$\Delta\sigma_{ord} = 0.81M\frac{\gamma_{APB}}{2b}\left(\frac{3\pi\phi}{8}\right)^{1/2}, \tag{1A}$$

where $M = 3.06$ is the mean matrix orientation factor for Al [91], $b = 0.286$ nm is the magnitude of the matrix Burgers vector [92], ϕ is the volume fraction of precipitates and $\gamma_{APB} = 0.5$ J m^{-2} is an average value of the Al_3Sc antiphase boundary (APB) energy for the (1 1 1) plane [93–95].

The increase in yield strength due to coherency strengthening is given by:

$$\Delta\sigma_{coh} = M\alpha_\varepsilon(G\varepsilon)^{3/2}\left(\frac{\langle R\rangle\phi}{0.5Gb}\right)^{1/2}, \tag{2A}$$

where $\alpha_\varepsilon = 2.6$ is a constant [89], $\langle R\rangle$ is the mean precipitate radius, $G = 25.4$ GPa [92] is the shear modulus of Al, ε is the constrained lattice parameter mismatch, taken to be that of Al_3Zr ($L1_2$) in Al ($\varepsilon = +0.88\%$ [1]) to approximate the Zr-enriched shell that envelopes the precipitates. This

provides a lower bound for the coherency-strengthening increment, since Al_3Sc ($L1_2$) and Al_3Er ($L1_2$) have higher constrained lattice parameter mismatches than Zr. The calculation of an upper bound for coherency strengthening is unnecessary since the Orowan bypass mechanism requires a lower stress than the calculated lower bound for $\Delta\sigma coh$ (Table 5) and is therefore the dominant precipitation-strengthening mechanism for all peak-aged samples.

Strengthening by modulus mismatch is given by:

$$\Delta\sigma_{mod} = 0.0055M(\Delta G)^{3/2}\left(\frac{2\phi}{Gb^2}\right)^{1/2} b\left(\frac{\langle R\rangle}{b}\right)^{\left(\frac{3m}{2}-1\right)}, \qquad (3A)$$

where $\Delta G = 42.5$ GPa is the shear modulus mismatch between the matrix and the precipitates [96], and m is a constant taken to be 0.85 [89].

Finally, the increase in yield strength for the Orowan bypass mechanism is given by:

$$\Delta\sigma_{Or} = M\frac{0.4}{\pi}\frac{Gb}{\sqrt{1-v}}\frac{\ln\left(\frac{\sqrt[2]{2/3}\langle R\rangle}{b}\right)}{\lambda}, \qquad (4A)$$

where $v = 0.34$ is the Poisson's ratio of the matrix [91] and λ is the interprecipitate distance, which is taken as the square lattice spacing in parallel planes [97]:

$$\lambda = \left[\left(\frac{3\pi}{4\phi}\right)^{1/2} - 1.64\right]\langle R\rangle. \qquad (5A)$$

References

[1] Knipling KE, Dunand DC, Seidman DN. Z Metallkd 2006;97:246.
[2] Marquis EA, Seidman DN. Acta Mater 2001;49:1909.
[3] Seidman DN, Marquis EA, Dunand DC. Acta Mater 2002;50:4021.
[4] Royset J, Ryum N. Int Mater Rev 2005;50:19.
[5] Drits ME, Ber LB, Bykov YG, Toropova LS, Anastas'eva GK. Phys Met Phys Metall 1984;57:1172.
[6] Drits ME, Dutkiewicz J, Toropova LS, Salawa J. Cryst Res Technol 1984;19:1325.
[7] Sawtell RR, Morris J. Exploratory alloy development in the system Al–Sc–X. In: Kim Y-W, Griffith WM, editors. Dispersion strengthened aluminum alloys. Warrendale, PA: TMS; 1988. p. 409.
[8] Elagin VI, Zakharov VV, Pavlenko SG, Rostova TD. Phys Met Phys Metall 1985;60:97.
[9] Tolley A, Radmilovic V, Dahmen U. Scripta Mater 2005;52:621.
[10] Forbord B, Lefebvre W, Danoix F, Hallem H, Marthinsen K. Scripta Mater 2004;51:333.
[11] Clouet E, Lae L, Epicier T, Lefebvre W, Nastar M, Deschamps A. Nat Mater 2006;5:482.
[12] Clouet E, Nastar M, Sigli C. Phys Rev B 2004;69:064109.
[13] Fuller CB, Murray JL, Seidman DN. Acta Mater 2005;53:5401.
[14] Fuller CB, Seidman DN. Acta Mater 2005;53:5415.
[15] Toropova LSED, Kharakterova M, Dobatkina T. Advanced aluminum alloys containing scandium: structure and properties. New York: Gordon and Breach Science Publishers; 1998.
[16] Clouet E, Nastar M, Barbu A, Sigli C, Martin G. Adv Eng Mater 2006;8:1228.
[17] Clouet E, Nastar M, Barbu A, Sigli C, Martin G. In: Solid-solid phase transformations in inorganic materials, vol. 2. TMS; 2005. p.683.
[18] Lefebvre W, Danoix F, Hallem H, Forbord B, Bostel A, Marthinsen K. J Alloys Compd 2009;470:107.
[19] Clouet E, Barbu A, Lae L, Martin G. Acta Mater 2005;53:2313.
[20] Hallem H, Lefebvre W, Forbord B, Danoix F, Marthinsen K. Mater Sci Eng A 2006;A421:154.
[21] Karnesky RA, Dunand DC, Seidman DN. Acta Mater 2009;57:4022.
[22] Karnesky RA, Seidman DN, Dunand DC. Mater Sci Forum 2006;519–521:1035.
[23] Karnesky RA, van Dalen ME, Dunand DC, Seidman DN. Scripta Mater 2006;55:437.
[24] Krug ME, Werber A, Dunand DC, Seidman DN. Acta Mater 2009;58:134.
[25] van Dalen ME, Karnesky RA, Cabotaje JR, Dunand DC, Seidman DN. Acta Mater 2009;57:4081.
[26] Harada Y, Dunand DC. Intermetallics 2008;17:17.
[27] vanDalen ME, Gyger T, Dunand DC, Seidman DN. Acta Mater, submitted for publication.
[28] Hedrick JB. US geological survey 2007. Minerals yearbook: rare earths; 2007.
[29] Zalutskaya OI, Ryabov VR, Zalutskii II. Dopov Akad Nauk Ukr RSR Ser A 1969;31:255.
[30] Marquis EA, Dunand DC. Scripta Mater 2002;47:503.
[31] Knipling KE, Dunand DC, Seidman DN. Acta Mater 2011;59:943.
[32] Knipling KE, Karnesky RA, Lee CP, Dunand DC, Seidman DN. Acta Mater 2010;58:5184.
[33] Fuller CB, Seidman DN, Dunand DC. Scripta Mater 1999;40:691.
[34] Fuller CB, Seidman DN, Dunand DC. Acta Mater 2003;51:4803.
[35] Belov NA, Alabin AN, Eskin DG, Istomin-Kastrovskii VV. J Mater Sci 2006;41:5890.
[36] Lohar AK, Mondal B, Rafaja D, Klemm V, Panigrahi SC. Mater Charact 2009;60:1387.
[37] Smola B, Stulikova I, Ocenasek V, Pelcova J, Neubert V. Mater Sci Eng A 2007;A462:370.
[38] Vlach M, Stulikova I, Smola B, Zaludova N, Cerna J. J Alloys Compd 2009;492:143.
[39] Kamardinkin AN, Dobatkina TV, Rostova TD. Izv Akad Nauk SSSR Met 1991:214.
[40] Davydov VG, Elagin VI, Zakharov VV, Rostova TD. Metalloved Term Obrab Met 1996:25.
[41] Bajikar SS, Larson DJ, Kelly TF, Camus PP. Ultramicroscopy 1996;65:119.
[42] Kelly TF, Camus PP, Larson DJ, Holzman LM, Bajikar SS. Ultramicroscopy 1996;62:29.
[43] Kelly TF, Larson DJ. Mater Charact 2000;44:59.
[44] Seidman DN. Rev Sci Instrum 2007;78:030901/1.
[45] Bunton JH, Olson JD, Lenz DR, Kelly TF. Microsc Microanal 2007;13:418.
[46] Seidman DN. Annu Rev Mater Res 2007;37:127.
[47] Kelly TF, Miller MK. Rev Sci Instrum 2007;78:031101.
[48] Hellman OC, Vandenbroucke JA, Rusing J, Isheim D, Seidman DN. Microsc Microanal 2000;6:437.
[49] Hellman OC, Blatz du Rivage J, Seidman DN. Ultramicroscopy 2003;95:199.
[50] Parratt LG. Probability and experimental errors in science. New York: John Wiley; 1966.
[51] Marumo T, Fujikawa S, Hirono K. J Jpn Inst Met 1973;23:17.
[52] Fujikawa S. Diffus Def Data A 1997;115:143–7.
[53] Karnesky RA. Mechanical properties and microstructure of Al–Sc with rare-earth element or Al_2O_3 additions. PhD thesis, Northwestern University, Evanston, IL; 2007. p. 258.
[54] Monachon C, Dunand DC, Seidman DN. Small 2010;6:1728.
[55] Monachon C, Krug ME, Dunand DC, Seidman DN. Acta Mater, submitted for publication.
[56] Radmilovic V, Tolley A, Marquis EA, Rossell MD, Lee Z, Dahmen U. Scripta Mater 2008;58:529.
[57] Mao Z, Booth-Morrison C, Seidman DN, Wolverton C. in preparation.
[58] van Dalen ME, Dunand David C, Seidman David N. J Mater Sci 2006;41:78814.

[59] Martin G. The theories of unmixing kinetics of solid solutions. Solid state phase transformation in metals and alloys. Orsay: Les Éditions de Physique; 1978. p. 337.
[60] Russell KC. Adv Colloid Interface Sci 1980;13:205.
[61] Wagner R, Kampmann R, Voorhees PW. Homogeneous second-phase precipitation. In: Kostorz G, editor. Phase transformations in materials. Weinheim: Wiley-VCH; 2001. p. 724.
[62] Kashchiev D. Nucleation: basic theory and applications. Oxford: Elsevier Science; 2000.
[63] Brechet Y, Martin G. CR Phys 2006;7:959.
[64] Asta M, Ozolins V, Woodward C. JOM 2001;53:16.
[65] Asta M, Foiles SM, Quong AA. Phys Rev B 1998;57:11265.
[66] Hyland Jr RW, Asta M, Foiles SM, Rohrer CL. Acta Mater 1998;46:3667.
[67] Watanabe C, Kondo T, Monzen R. Metall Mater Trans A 2004;35A:3003.
[68] Asta M, Ozolins V. Phys Rev B 2001;64:094104.
[69] Fu CL. J Mater Res 1990;5:971.
[70] Xu J, Freeman AJ. Phys Rev B 1990;41:12553.
[71] Cacciamani G, Riani P, Borzone G, Parodi N, Saccone A, Ferro R, et al. Intermetallics 1998;7:101.
[72] Gao MC, Rollett AD, Widom M. Phys Rev B 2007;75:174120.
[73] Murray JL. J Phase Equilib 1998;19:380.
[74] Lee JK. Theor Appl Fract Mech 2000;33:207.
[75] Hyland Jr RW, Stiffler RC. Scripta Metall Mater 1991;25:473.
[76] Okamoto H. Phase diagrams of dilute binary alloys. Materials Park, OH: ASM International; 2002.
[77] Murray JL, Peruzzi A, Abriata JP. J Phase Equilb 1992:13.
[78] Massalski TB, editor. Binary alloy phase diagrams. Materials Park, OH: ASM International; 1990.
[79] Iwamura S, Miura Y. Acta Mater 2004;52:591.
[80] Riddle YW, Sanders Jr TH. Mater Sci Forum 2000;939:331–7.
[81] Jones MJ, Humphreys FJ. Acta Mater 2003;51:2149.
[82] Royset J, Ryum N. Scripta Mater 2005;52:1275.
[83] Berezina AL, Volkov VA, Domashnikov BP, Ivanov SV, Chuistov KV. Phys Met 1990;12:72.
[84] Harada Y, Dunand DC. Mater Sci Eng A 2002;686:A329–31.
[85] Harada Y, Dunand DC. Scripta Mater 2003;48:219.
[86] Tabor D. Brit J Appl Phys 1956;7:159.
[87] Marquis EA, Seidman DN, Dunand DC. Acta Mater 2003;51:285.
[88] van Dalen ME, Seidman DN, Dunand DC. Acta Mater 2008;56:4369.
[89] Ardell AJ. Metall Trans A 1985;16A:2131.
[90] Argon A. Strengthening mechanisms in crystal plasticity. Oxford: Oxford University Press; 2007.
[91] Meyers M, Chawla K. Mechanical metallurgy: principles and applications. Englewood Cliffs, NJ: Prentice Hall; 1984.
[92] Frost H, Ashby M. Deformation mechanism maps. Oxford: Pergamon Press; 1982.
[93] Fu C. J Mater Res 1990;5:971.
[94] George E, Pope D, Fu C, Schneibel J. ISIJ Int 1991;31:1063.
[95] Fukunaga K, Shouji T, Miura Y. Mater Sci Eng 1997;A239:202.
[96] Hyland R, Stiffler R. Scripta Metall Mater 1991;25:473.
[97] Nembach E. Particle strengthening of metals and alloys. New York: John Wiley; 1997.